# Three-Dimensional Particle Simulation of Plume Flows From Hall Thrusters

**IEPC-2005-048**

*Presented at the 29$^{th}$ International Electric Propulsion Conference, Princeton University October 31 – November 4, 2005*

Chunpei Cai*, Iain D. Boyd† and Quanhua Sun‡
*University of Michigan, Ann Arbor, Michigan, 48109, U.S.A*

**Abstract: In this study, three-dimensional simulations of xenon plasma plume flow fields from a cluster of four Hall thrusters are performed with a hybrid particle-fluid method on unstructured meshes. In these simulations, a detailed fluid model is used to compute the electron properties, the direct simulation Monte Carlo method models the collisions of heavy particles and the Particle-In-Cell method models the transport of ions in electric fields. Facility effects of large vacuum chambers are briefly discussed and the background flow treatment in the particle simulations fully considers these effects, including the vacuum pump sticking coefficient, the pump size the pump temperature and the wall temperature. The accuracy of the simulations is assessed through comparisons with available measured data. The simulations successfully capture detailed three-dimensional plume structures and plume interactions. The results indicate that the cathode has effects on some flow properties in the field close to the thrusters.**

*Graduate Student Research Assistant, Department of Aerospace Engineering, ccai@engin.umich.edu.
†Professor, Department of Aerospace Engineering, iainboyd@umich.edu.
‡Research Associate, Department of Aerospace Engineering, qsun@engin.umich.edu, now in CFD-RC.

## Nomenclature

| | |
|---|---|
| $a_i$ | = coefficient for the $i$th node in a tetrahedral cell |
| $b$, $a$, $d$ | = $x$, $y$, $z$ distances from a cathode to the cluster center |
| $d$ | =atomic diameter |
| $c_e$ | =mean electron thermal velocity |
| $C_i$ | =ionization coefficient |
| $f(C)$ | =velocity distribution function |
| $e$ | =unit charge |
| $\overrightarrow{E}$ | =electric field vector |
| $g$ | =relative velocity |
| $J$ | =free charge current density |
| $J_A$ | =anode electron current density |
| $J_C$ | =cathode current density |
| $k$ | =Boltzmann constant |
| $Kn$ | =Knudsen number |
| $\dot{m}$ | =mass flux rate into vacuum chamber |
| $m$ | =mass |
| $m_c$ | =reduced mass |
| $n$ | =plasma number density, or number of nodes |
| $n_a$ | =neutral number density from anode |
| $n_{back}$ | =background neutral density |
| $n_c$ | =neutral number density from cathode |
| $n_{in}$ | =number density for flux into the vacuum chamber |
| $n_x$, $n_y$, $n_z$ | =normal of cathode exit plane |
| $\overrightarrow{n}$ | =surface normal |
| $p_e$ | =electron pressure |
| $P_b$ | =chamber backpressure |
| $P(x, y, z)$ | =variable for the generalized Poisson equations |
| $Q(x, y, z)$ | =coefficients for the generalized Poisson equations |
| $\overrightarrow{r}$ | =distance vector between two points |
| $R_c$ | =cathode orifice radius |
| $R$ | =gas constant |
| $s$ | =area ratio, $= S_p/S_c$ |
| $S_p$ | =pump surface area |
| $S_c$ | =chamber cross-section area |
| $S(x, y, z)$ | =source terms for the generalized Poisson equations |
| $T$ | =temperature |
| $T_H$ | =heavy particle temperature |
| $V$ | =cell or chamber volume |
| $\alpha$ | =pump sticking coefficient |
| $\gamma$ | =specific heat ratio |
| $\sigma$ | =plasma conductivity |
| $\sigma_i$ | =reference cross section for xenon |
| $\sigma_{el}$ | =reference cross section for elastic collisions |
| $\theta_+$ | =divergence angle for the outer channel edge |
| $\theta_-$ | =divergence angle for the inner channel edge |
| $\kappa_e$ | =electron thermal conductivity |

$\epsilon_i$ =ionization energy for xenon, =12.7 eV
$\phi$ =plasma potential
$\rho$ =background density
$\rho_0$ =initial background density
$\omega$ =viscosity temperature exponent
$\Omega$ =solid angle in velocity phase space or physical space
$\nu_e$ =electron collision frequency, $= \nu_{ei} + \nu_{en}$
$\nu_{ei}$ =ion-electron collision frequency
$\nu_{en}$ =neutral-electron collision frequency
$\psi$ =electron velocity stream function

subscript

$_{ref}$ reference value
$_i$ ion
$_e$ electron
$_n$ neutrals
$_p$ pump
$_w$ chamber wall

# I. Introduction

Hall thrusters represent a very efficient form of electric propulsion devices widely used on spacecraft for on-orbit applications such as station keeping. In general, Hall thrusters are replacing chemical thrusters in specific applications because of several merits. Hall thrusters can create higher specific impulse, obtain electricity input directly in space through solar cells, and do not require carrying oxidant. High power electric propulsion systems are being investigated due to improvements in solar cell technology and due to renewed interest in nuclear power.

The development of high-power Hall thrusters falls into two categories: one case involves investigating single, monolithic thrusters, while the second case involves clustering several small thrusters. Generally, clustering is favorable because of several merits including a cheaper manufacturing cost, less demanding requirement from test facilities, more robustness and an ability to tolerate failure of single thrusters.

There are several major interests in numerical simulation of plasma flows from a cluster of Hall thrusters. One interest is to investigate the plume interactions, especially in the complex and important near field locations. The performance of a thruster in a cluster may be different from a stand alone situation. Another interest is to estimate plume impingement, which involves high-energy ions and charge exchange ions (CEX), onto sensitive spacecraft surfaces such as solar arrays. When a fast ion collides with a slow neutral, one or two electrons may transfer from the neutral to the ion, resulting in a slow ion and a fast neutral. Under the electric field, this ion may drift behind the thruster. Severe impingement of ions onto spacecraft surfaces may result eventually in failure of devices or even a final failure of the whole mission. If severe impingement is predicted, then a change of design philosophy must be considered to reduce the impingement.

To accurately simulate the plasma plumes from a cluster of Hall thrusters requires an accurate modeling of the complex physical plume mechanism on three-dimensional meshes. A plasma plume is a complex rarefied flow with several species: atoms, positively charged ions and negatively charged electrons. Traditionally, the computational simulation of plasma plume flows into vacuum is performed with a hybrid particle-fluid approach. The direct simulation Monte Carlo (DSMC) method[1] models the collisions of the heavy particles (ions and atoms) while the Particle In Cell (PIC) method[2] models the transport of the ions in electric fields. The electrons are modeled using a fluid description because they adjust their velocities more quickly with their significantly lighter mass. Due to the clustering effects, plumes from different thrusters may interact with each other. In addition the cathode-neutralizers also produce three dimensional effects. To accurately simulate the plume flows, 3D unstructured meshes must be adopted.

For the fluid electron model, a recently proposed detailed fluid electron model by Boyd and Yim[3] has

many advantages over a Boltzmann relation, which is widely adopted to compute the plasma potential. The Boltzmann relation has many assumptions such as a constant electron temperature distribution. The detailed fluid electron model by Boyd and Yim[3] was based on the conservation laws for electrons and is capable of providing accurate and detailed distributions for electron temperature, plasma potential and electron velocity. This model was successfully applied in a simulation of an axi-symmetric plasma plume from a 200 W class Hall thruster. In this study, the three-dimensional plume flow fields from a cluster of four 200 W class Hall thrusters are simulated with the DSMC-PIC methods and the detailed fluid electron model using unstructured three-dimensional meshes.

Section II briefly introduces background information from experiments; section III reviews the general DSMC-PIC hybrid methods with several numerical implementation issues; section IV briefly discusses the facility effects of a large vacuum chamber and a special numerical treatment of background flow in the simulations, and finally section V presents three-dimensional simulations and a discussion of results.

## II. Background

The devices considered in the present study are a cluster of four BHT-200 Hall thrusters manufactured by Busek, Co. Each thruster is operated at 200 W with a nominal thruster level of 13 mN. The cluster of BHT-200 thrusters has been investigated experimentally.[4,5]

The data in Ref. 5 were taken in a cylindrical chamber with a length of 9 m and a diameter of 6 m at the Plasmadynamics and Electric Propulsion Laboratory (PEPL) at the University of Michigan and Fig.1 is a photograph of the thrusters in operation. In this large stainless steel chamber, 7 two-sided cryogenic pumps are installed near one chamber end. These pumps are maintained at a low temperature of $T_w$=12 K 15 K by gaseous helium, and when atoms hit the pumps, by a probability of $\alpha$ they will stick to the pump, and a probability of $1-\alpha$ they will rebound with a thermal velocity characterized by the pump temperature $T_w$. The four thrusters are configured in a 2 by 2 grid with a center-to-center distance of 0.115 m. In the following simulations, the same thruster numbering as Ref.5 is adopted: the upper left, lower left, lower right and upper right thrusters are named as thruster 1, 2, 3 and 4. As shown in the same photograph, there are four cathode-neutralizers located either above or at the bottom of each thruster, and there is a 7 mm conic cap on the front face of each thruster to protect the thruster against ion sputtering. Due to the symmetry, only one thruster and one cathode are needed in the three-dimensional simulations.

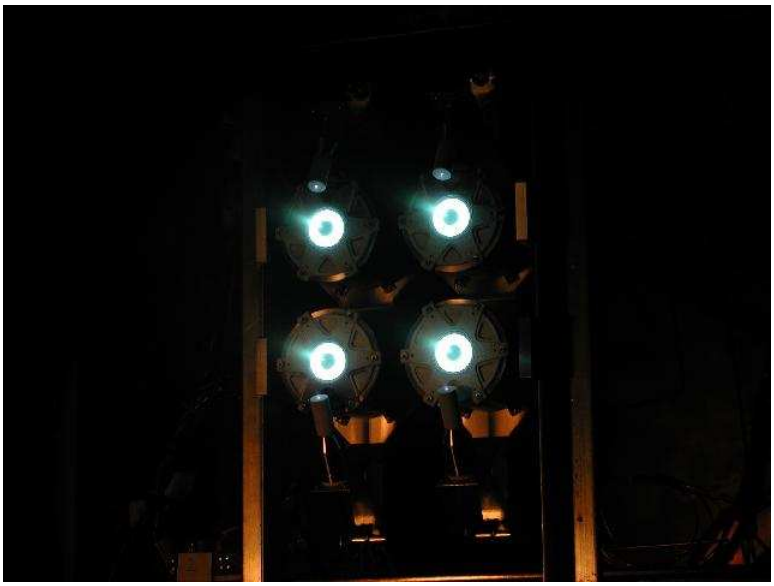

**Figure 1. Four BHT-200 Hall Thrusters in Operation(Courtesy of PEPL).**

The total pumping speed in this facility for these experiments was 140,000 l/s on xenon resulting in a backpressure of $1.1 \times 10^{-6}$ Torr. Faraday probes were used to measure angular profiles of ion current density. A retarding potential analyzer was also used to measure the ion energy distribution function in the

plume far field. In addition, a floating emissive probe and a triple Langmuir probe were used to measure the plasma potential, the electron number density and the electron temperature. Xenon is adopted for plasma propellant. A plume from a plasma thruster consists of light electrons with speeds of $1 \times 10^6$ m/s, and heavier ions or neutrals, such as fast single or double charged ions, $Xe^+$, $Xe^{++}$, slow neutral xenon, and fast neutral xenon and slow ions due to CEX.

## III. Simulation Methods and Numerical Implementation Issues

### A. General Steps for the DSMC-PIC Methods

For particle simulations of plasma plume flow, heavy neutrals and ion particles are simulated with the DSMC[1] and the PIC[2] methods, while the electrons are modeled as a fluid because electrons can adjust themselves more quickly. The hybrid DSMC-PIC simulation can be summarized with the following steps:

Step 1. (PIC): Allocate the charge of each ion inside a cell onto the cell nodes.

Step 2. (Fluid): Calculate plasma potential $\phi$ using a fluid electron model.

Step 3. (PIC): Calculate ionization in all cells. A fraction of neutrals will be changed to ions.

$$\Delta n_i = C_i n_a n_i \Delta t \tag{1}$$

Step 4. (PIC): Calculate the electric field on each node with the relation:

$$\overrightarrow{E} = - \bigtriangledown \phi \tag{2}$$

Step 5. (DSMC, PIC): Sample quantities inside each cell.

Step 6. (DSMC): Perform momentum exchange and CEX collisions inside each cell.

Step 7. (DSMC, PIC): Introduce new particles (ions and neutrals) into the simulation domain from inlet boundaries.

Step 8. (PIC): Calculate the ion acceleration based on its location inside its cell.

Step 9. (DSMC, PIC): Move all particles with the time step. When particles move across an outer boundary, they are removed from the simulation; when a neutral particle collides with thruster walls, it rebounds back into the simulation domain with a thermal velocity characterized by the wall temperature of 300 K; when an ion collides with the wall, it regains its charge and rebounds as a neutral.

In this study, magnetic field effects are neglected because the magnetic field leakage is only expected to be significant right next to the thruster.

### B. The Detailed Fluid Electron Model

In the first PIC step to compute the plasma potential, the simplest and most widely used fluid electron model is the Boltzmann relation, which is obtained from the electron momentum equation:

$$\phi = \phi_{ref} + \frac{kT_{ref}}{e} \log(\frac{n_e}{n_{ref}}) \tag{3}$$

However, this equation is derived using several strong assumptions. These assumptions include that the fluid electron flow is isothermal, collisionless, the electron pressure obeys the ideal gas law and the magnetic field is neglected. In plasma plumes, especially in the near field, there are significant gradients and the approximation may be inappropriate.

To improve the understanding of the plume flow characteristics, recently a detailed electron model was proposed[3] and illustrated with an axi-symmetric plume simulation and the major results are summarized here for reference.

In the detailed model, an equation for the electron stream function $\psi$ can be derived from the steady mass conservation law for electrons with ionization effects and the final expression is:

$$\nabla^2 \psi = n_e n_a C_i \tag{4}$$

where $n_e \overrightarrow{v}_e = \nabla \psi$ and the ionization rate coefficient $C_i$ is expressed as a function of electron temperature using a simple relation proposed by Adeho et al.[6]:

$$C_i = \sigma_i c_e \big(1 + \frac{T_e \epsilon_i}{(T_e + \epsilon_e)^2}\big) \exp(-\frac{\epsilon_i}{T_e}) \tag{5}$$

From a generalized Ohm's law:

$$\overrightarrow{j} = \sigma[-\nabla\phi + \frac{1}{en_e}\nabla(n_e k T_e)] \tag{6}$$

with known $n_e$, $\overrightarrow{v_e}$, $T_e$ and the charge continuity condition:

$$\nabla \cdot \overrightarrow{j} = 0 \tag{7}$$

a generalized Poisson's equation describing the electron potential is obtained:

$$\nabla \cdot (\sigma\nabla\phi) = \frac{k}{e}\big(\sigma\nabla^2 T_e + \sigma T_e \nabla^2(\ln(n_e)) + \sigma\nabla(\ln n_e)\cdot\nabla T_e + T_e\nabla\sigma\cdot\nabla(\ln(n_e)) + \nabla\sigma\cdot\nabla T_e\big) \tag{8}$$

The electron temperature equation is obtained from the steady state electron energy equation:

$$\nabla^2 T_e = -\nabla\ln(\kappa_e)\cdot\nabla T_e + \frac{1}{\kappa_e}\big(-\overrightarrow{j}\cdot\overrightarrow{E} + \frac{3}{2}n_e(\overrightarrow{v_e}\cdot\nabla)kT_e + p_e\nabla\cdot\overrightarrow{v_e} + 3\frac{m_e}{m_i}\nu_e n_e k(T_e - T_h) + n_e n_a C_i\epsilon_i\big) \tag{9}$$

The electron number density $n_e$ is set equal to the ion number density $n_i$ based on the plasma quasi-neutral assumption. The electron conductivity $\sigma$, the electron thermal conductivity $\kappa_e$, the ion-electron collision frequency $\nu_{ei}$, and the neutral electron collision frequency $\nu_{en}$ can be found in Ref. 7 and its references:

$$\sigma = \frac{e^2 n_e}{m_e \upsilon_e} \tag{10}$$

$$\kappa_e = \frac{2.4}{1 + \frac{\nu_{ei}}{\sqrt{2}\nu_e}}\frac{k^2 n_e T_e}{m_e \nu_e} \tag{11}$$

where $\nu_e = \nu_{ei} + \nu_{en}$, $\nu_{ei}$ is the ion-electron collision frequency, $\nu_{en}$ is the neutral electron collision frequency.

By treating the right hand side terms as known sources and solving Equations 4, 8, and 9, three fundamental electron properties are obtained, i.e., electron velocity, plasma potential, and electron temperature. With these detailed properties, the plasma plume simulation yields much improved results in comparison to the Boltzmann relation.

### C. General Finite Element Solver for Poisson Equations

Each of Equations 4, 8 and 9 can be expressed as a general Poisson equation[8]:

$$-\bigtriangledown\big(P(x,y,z)\bullet\bigtriangledown Q(x,y,z)\big) = S(x,y,z) \tag{12}$$

where $P(x,y,z)$ is a distribution of coefficients, $Q(x,y,z)$ is a distribution of the primary variable to be solved and $S(x,y,z)$ is a known distribution of source terms.

For a two-dimensional or axi-symmetric simulation on a structured mesh, an Alternative Direction Implicit(ADI) iterative solver[9] is usually adopted for simplicity. However, there are several drawbacks for the ADI method:

i). It is not applicable, or is very difficult to implement, on unstructured meshes.

ii). For a structured mesh, depending on the geometry of the simulation domain, the ADI method needs to be applied on each sub-domain separately with artificial inner boundaries which may result in inaccuracy in the simulation results. This precludes the application of ADI to complex geometries, even with structured meshes.

iii). The treatment of boundaries is not natural. This may result in inaccuracies for the source terms on the first layer of nodes on boundaries. At the thruster exit, the gradients are significant and a mistreatment of boundary source conditions will spread the effects into the whole flow domain because of the elliptical property of these equations. The first three layers of nodes close to the boundaries will be heavily affected.

To simulate flows with very complex geometry, an unstructured mesh must be adopted and this actually precludes the ADI method. To address the above problems, a general purpose finite element solver applicable to two- and three-dimensional structured and unstructured meshes is developed to solve the above three equations. Compared with the ADI method, the finite element method is applicable on structured and unstructured meshes and can integrate the boundary conditions more naturally and accurately.

The discrete, stiff matrix for a triangular cell can be found in Ref. 8, and a quadrilateral cell can be simply assembled as two triangles. For a three-dimensional tetrahedral cell, the discretization process and boundary condition treatment can found in Ref.10.

The final global stiff matrix is sparse, symmetric and positive definite. These novel properties are not naturally guaranteed by a finite difference method or a finite volume method. To fully take advantage of these properties, an efficient storage scheme[9] is adopted which only requires a cost of $O(n)$ where $n$ is the total node number. The iterative conjugate gradients method[9] is adopted to solve the final linear equations. This method fully takes advantage of the sparse, symmetric and positive definite properties of the global stiff matrix.

### D. Derivative Calculation on an Unstructured Mesh

Several situations will require the calculation of derivatives on a node. Two situations are Step 2 to calculate the source terms for Equations 4, 8, 9, and Step 3 to calculate the electric field from a potential field. Besides accuracy, one requirement for the optimal calculation scheme is to be applicable on both serial and parallel machines.

There are several options to calculate derivatives on unstructured meshes and one of them is the least square method[10]. The basic idea of the least square method can be illustrated with an example to calculate the electric field from a potential field: assume the unknown gradients on one node are $\vec{E}(x, y, z) = (E_x, E_y, E_z)$, if there are $N$ nodes connected to this node with differences of plasma potential $d(\phi)_i$ and distance vectors $dX_i$, then they form $N \times 3$ relations which are over-determined:

$$ME = d\phi \tag{13}$$

where $M$ is an $N \times 3$ matrix, $E$ is a $3 \times 1$ vector, and $d\phi$ is an $N \times 1$ vector. By multiplying by a transposed matrix $M^T$ on both sides, this over-determined matrix is transformed to a $3 \times 3$ matrix and the equations are solvable.

One tetrahedral cell is generally enough to decide the derivatives on a specific cell node, and this scheme yields accurate results by including the effects from all nodes connected to a specific node. The least square method is also applicable on parallel machines. The only extra cost of this scheme is, at the beginning of a simulation, a table of node connection relations must be gathered and saved for the whole simulation process.

### E. Weighting Schemes

A weighting scheme is crucial for a successful DSMC-PIC simulation with the detailed fluid electron model because several critical steps use the weighting scheme. In Step 1, the ion number density at a specific node must be accurately estimated by weighting the charge of ions in all cells connected with this node. In Step 8, the acceleration for a particle is interpolated from the electric field values on the same nodes. Generally, these two weighting schemes are preferably the same, and the closer a particle to a node, the more influence this particle will have on or from the node. In Step 3, a correct ionization source term requires both valid charge density and valid neutral density allocated from particles to cell nodes as well.

Usually for charge allocation, there exists two categories of weighting schemes. The first category of weighting schemes is based on areas or volumes. In these methods, a particle's charge is allocated to cell nodes by the areas or volumes formed by the particle's position in the cell nodes. The particle's position in a cell does have an important influence on the weight of its charge to be assigned on different cell nodes. This scheme is expected to yield a higher accuracy and is very widely used in PIC simulations. For example, Ruyten[11] presented a well-used scheme for structured axi-symmetric meshes that works accurately on cylindrical coordinates with structured rectangular cells by satisfying both charge conservation and charge density conservation. In the literature, there are reports that use similar weighting schemes on unstructured meshes based on volumes and areas. However, it will be shown later this is not a proper scheme for a DSMC-PIC simulation of plasma flows on unstructured meshes, especially with the detailed fluid electron model or ionization effects. The other category of weighting schemes is expected to have a lower degree of accuracy since a particle's position in a cell does not have an influence on its weights to different nodes, and density is not conserved. In this type of method, the charge density on a specific node is calculated by summing up all particles' charge inside a closed volume enclosing the node, then dividing by the volume. This closed volume can either be all the cells connected to this node, or, a fraction of these cells. Generally

this category of weighting schemes does not have problems associated with the first category, and they can be used for a DSMC-PIC simulation with unstructured meshes.

There are two problems associated with the weighting scheme based on areas or volumes on an unstructured mesh. Suppose there are a large number of particles in each cell and the average number density is $n$. Weighting by areas or volumes, similar to Ruyten's scheme, will approximately equally distribute the ion or neutral density onto the nodes forming this cell. Consider Figure 2, for a two-dimensional mesh, on the right, the center node is shared by four cells, and the total charge number density at the center node is $n/4 \times 4 = n$. While for the unstructured mesh on the left, the total charge number density will be $n/3 \times 6 = 2n$. While for three-dimensional unstructured tetrahedral cells, usually there are about 16 or more cells connected to an inner node, hence the number density at that node will be calculated as $n/4 \times 16 = 4n$. It is obvious that, for an unstructured mesh, if the weighting scheme by areas or volumes is applied, for a two-dimensional situation with triangles the charge density at one node will be two times higher than its real value, while for an unstructured three-dimensional situation, the estimated charge density will be four or five times higher than the real charge density, depending on how many neighboring cells are connected to this specific node. Another problem associated with the weighting scheme by areas or volumes is boundary

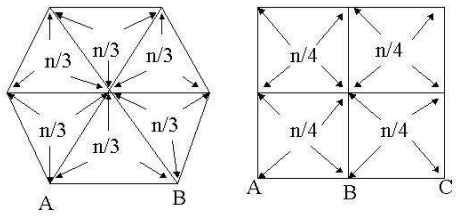


**Figure 2. Effects of Weighting Scheme by Area/Volume on Unstructured Meshes.**

treatment. In Figure 2, the number density at a boundary node may be incorrect with a scheme based on volume or area. For example, if node B in the picture on the right is on a boundary, then with a weighting scheme based on areas or volumes, the number density on node B will be $n/4 \times 2 = n/2$. Compensations will be necessary to correct the number density for all the boundary nodes on the inlets, outlet, walls and symmetric axis. Failure to perform compensation may result in some subtle problems in the simulation results. For example, on the symmetric line of an axi-symmetric simulation, $E_y$ is usually correctly forced to be zero, but, some properties such as $E_x$ on the axis and $E_y$ on the layer of nodes next to the axis, and source terms on the axis will not be correct if the density on the axis is not compensated. Theoretically, a compensation of two times on the axis is only approximately correct for the axi-symmetric situation due to radial effects.

If the Boltzmann relation, Equation 3, is used to compute the plasma potential, the overestimated charge density may not result in significant problems. The mistake in plasma potential is globally offset by the logarithm function in Equation 3, and this error is further canceled in the calculation of the electric field by Equation 2. As a result, even though the number density and the plasma potential are calculated incorrectly by the weighting scheme of areas or volumes, the electric field is almost correct. This is the possible reason why there are no reports of this problem in the literature. However, weighting by areas or volumes for an unstructured mesh is not a correct approach and should be avoided.

For the detailed fluid electron model, which includes detailed physical terms and the potential is calculated by Equation 8, this mistake of over-estimated density will create a false potential field. Further, for the ionization source term in Equation 1, both the charge density and the neutral density on a node will be overestimated, and a minimum of $4 \times 4 - 1 = 15$ times higher source terms will be calculated for the ionization process in Step 2. In the near field, the neutral number density is usually much higher than the ion number

density, hence, an overestimated ionization rate will trigger a positive feedback for the ion number density. Finally, in the near field, a false high accumulation of ion number density will be generated and completely corrupt the potential field. For the detailed fluid electron model, where the potential calculation is more sensitive than the Boltzmann relation, the weighting scheme by areas or volume will trigger the chain reaction in ionization and finally invalidate the simulation. Hence, the first category of weighting schemes based on areas or volumes, is totally unusable on unstructured meshes for this detailed fluid model with ionization effects.

For the second category of weighting schemes, usually a correct charge allocation is always expected. In the literature, one option to calculate the charge density on a specific node is by summing up all particles inside the cells around the node then dividing by the total volume of all cells surrounding the node:

$$n = \sum_{j=0}^{N} N_j / \sum_{j=0}^{N} V_j \tag{14}$$

Hammel[12] reported another scheme which is similar but more accurate than Equation 14 and requires a high quality mesh. The total charge of a particle is assigned to the closest node from this particle. Though this scheme is physically accurate, there are situations when the nearest node to the particle is not one of the cell nodes forming the cell where the particle is located, such as regions near boundaries with boundary constraints. Hence, though more accurate, this algorithm is more difficult to implement.

The most common defect for the second category of weighting scheme is that it requires much cross node transportation on a parallel machine and it will be quite inefficient. The charge and neutral allocation scheme adopted in this study is a simple one. First, the cell average values are calculated and then these values are averaged onto the nodes in the current processor. Suppose there are $N$ cells connected to a node in one computer processor, and the $j$th cell has an average charge density $n_j$, then the charge density $n$ on the node can be expressed as:

$$n = \sum_{j=0}^{N} n_j / N \tag{15}$$

This scheme does not require a complete list of cell average values for all cells physically connected to a node, but only cells in the same computer processor, hence, it is efficient on a parallel machine without significant loss of accuracy. The interpolation of electric field with the weighting scheme by areas or volumes is still correct and no change is necessary.

To effectively suppress statistical scatter in the charge density, this study further adopts a relaxation in charge and ion density on a node:

$$n_{new} = 0.1 n_{alloc} + 0.9 n_{old} \tag{16}$$

where $n_{new}$ is the current charge or neutral number density, $n_{alloc}$ is the density obtained from the just mentioned allocation scheme, and $n_{old}$ is the charge or neutral number density used in the last time step. For steady flow simulations, this treatment is effective in reducing statistical scatter.

### F. Collision Dynamics

The DSMC method uses particles to simulate collision effects in rarefied gas flow by collecting groups of particles into cells that have a size of the order of a mean free path. In Step 6, pairs of particles inside a cell are selected at random and a collision probability is evaluated that is proportional to the product of the relative velocity and the collision cross section for each pair. The probability is compared with a random number to determine if that collision occurs. If so, some form of collision dynamics is performed to alter the properties of the colliding particles. The no time counter method[1] is adopted to determine if a collision occurs in this study. A special treatment to handle collisions between particles of different weight will be presented later.

There are two types of collisions that are important in these Hall thruster plumes: elastic, or momentum exchange(MEX) collisions and charge exchange (CEX)collisions. The elastic collisions involve only exchange of momentum between the participating particles. For atom-atom collisions, the Variable Hard Sphere[1] model is employed and the collision cross section of xenon is:

$$\sigma_{el}(Xe, Xe) = \frac{2.12 \times 10^{-18}}{g^{2\omega}} m^2 \tag{17}$$

where $g$ is the relative velocity and $\omega$=0.12 is related to the viscosity temperature exponent for xenon. For atom-ion elastic interactions, one common choice is to use the following cross section of Dalgarno et al.[13]:

$$\sigma_{el}(Xe, Xe^{+}) = \frac{2.12 \times 10^{-18}}{g} m^2 \tag{18}$$

Another choice, which is adopted in this study, is to set the MEX cross section equal to the CEX cross secti.

In all elastic interactions, the collision dynamics is modeled using isotropic scattering together with conservation of linear momentum and energy to determine the post-collision velocities of the colliding particles. Charge exchange concerns the transfer of one or more electrons between an atom and an ion. For singly and doubly charged ions, the following cross section measured by Pullins et al.[14] and Miller et al.[15] are used:

$$\sigma_{el}(Xe, Xe^{+}) = 1.0 \times 10^{-20}(87.3 - 13.6\log(\frac{m_c g^2}{2}))m^2 \tag{19}$$

$$\sigma_{el}(Xe, Xe^{++}) = 1.0 \times 10^{-20}(45.7 - 13.6\log(\frac{m_c g^2}{2}))m^2 \tag{20}$$

where $m_c$ is the reduced mass. It is assumed that there is no transfer of momentum accompanying the transfer of the electron(s). This assumption is based on the premise that charge exchange interactions are primarily at long range.

### G. Boundary Conditions

When an ion particle hits a wall, it loses its charge and reflects diffusely as a neutral particle with a thermal velocity characterized by a wall temperature of 300 K. For the thrusters in this study, the front wall and the center protection cap are dielectric, and the sheath voltage is significant. The sheath voltage for the front wall can be estimated by a transformation of Equation 6:

$$\phi_w = \phi_0 + \left( \frac{\overrightarrow{J}}{\sigma} - \frac{k \bigtriangledown (n_e T_e)}{e n_e} \right) \cdot d\overrightarrow{l} \tag{21}$$

where $\phi_0$ is the potential at the node next to the wall. For other wall locations, a potential of 0 Volt is appropriate. The gradient of electron temperature is set to zero at each wall.

Several macroscopic properties of the plasma are required as boundary conditions for the computations. Specifically, the plasma potential, the electron stream function and the electron temperature are required for all boundaries. Table 1 summarizes the boundary conditions for the stream function, the plasma potential and the electron temperature, most of these values are the same as the values in Ref.3.

| Boundary | Outflow | Wall | Thruster Exit | Cathode | Symmetric plane |
|---|---|---|---|---|---|
| $\phi(V)$ | 2 | 0 or Eqn.( 21) | 93.0 | 7.0 | $\frac{\partial \phi}{\partial n} = 0$ |
| $\Psi(m^{-1}s^{-1})$ | $\frac{\partial^2 \Psi}{\partial n^2} = 0$ | 0 | $\frac{\partial \Psi}{\partial n} = \frac{J_c}{e}$ | $\frac{\partial \Psi}{\partial n} = \frac{J_a}{e}$ | $\frac{\partial \Psi}{\partial n} = 0$ |
| $Te$(eV) | 0.6 | 1 | 6.0 | 2.0 | $\frac{\partial Te}{\partial n} = 0$ |

**Table 1. Boundary Conditions for the Detailed Electron Fluid Model.**

At the thruster exit, for all heavy species, the number density, velocity and temperature are required. The setup employs a mixture of analysis and estimation based on experimental data of the mass flow rate from anodes and cathodes, thrust, and total ion current. The neutrals are assumed to exit the thruster and cathodes at the sonic speed corresponding to assumed values for their temperature. Finally, a divergence angle of $\theta_+ = 30$ degree for the outer edge and $\theta_- =$20 degree for the inner edges of the exit channel are assumed. The thruster and the cathode wall temperature are set to 300 K.

### H. Particle Weight

In this study, the inlet boundary conditions have quite different scales and particle weight is adopted. For the cathode, the diameter is about $5.08 \times 10^{-4}$ m, though the neutral number density at the cathode exit

is greater than that at the anode exit, the fluxes of ions and neutrals from the cathode are smaller than those from the anode. To address this problem, particle weighting is enabled in the code. Each particle introduced at the cathode and anode is assigned with a relative weight ratio $W_p$. The real particle weight is decided by multiplying this $W_p$ with the local cell weight ratio $W_c$. When particles travel from one cell into another, a clone process is performed based on the two cell weight ratios, and this particle's relative ratio does not change. Background static particles are assigned with weight ratios as well. This treatment effectively resolves the problem of different fluxes from cathodes and anodes.

One issue for this different particle weighting is collisions, and it is handled using the following procedure: when two particles collide, the heavier particle is split into two particles: one split particle has the same weight ratio as the other particle and a collision is performed between these two particles with the same weight; the other split particle keeps the rest of the weight and does not participate in collision. This treatment is quite similar to Ref.16, which reported a simulation of flows with trace species.

Collisions with background static particles should be handled carefully. In axi-symmetric simulations and three-dimensional simulations, cell volumes change dramatically. For example, in the former case, cells with a large radius have a large volume while cells around the axis have quite small volumes. In these three-dimensional simulations, cells at the outer boundary and cells around the cathodes have quite different cell volumes. The relative particle weights for the background static particles are quite different, and can be much smaller than those for a normal particle. When a normal particle and a background static particle collide, if the normal particle's weight ratio is greater than the static particle, then a split of the normal particle should be processed. Failure to perform this process results in a false velocity change for the normal particle.

Though this splitting scheme is quite effective for the problems in this study, it results in an increasing number of low-weight particles due to collisions. For neutral particles, a special process is implemented to reduce their number: if a neutral particle's relative weight $W_p$ is larger than a threshold value $W_{thresh}$, it is kept in the simulation without a weight change; otherwise, it is either discarded from the simulation, or kept in the simulation statistically by changing its relative weight ratio to the threshold value. For ion particles, they are essential to the simulations, hence their weights are unchanged and all ions are kept in the simulation. For DSMC-PIC simulations with background static particles representing a finite backpressure, the process is like a slow diffusion process: a large amount of slow ions slowly diffusing in the simulation domain. This represents a problem to be addressed in a future study.

In this study, a specific DSMC package MONACO[17] is used to perform all DSMC-PIC hybrid simulations.

## IV. Large Vacuum Chamber Facility Effects and Backpressure Treatment

One novel aspect of the simulations is that background pressure and facility effects are considered. EP devices are designed for use in space, where almost perfect vacuum exists, but they are tested in ground vacuum chambers such as the LVTF, where a finite background chamber pressure always exists and that may result in adverse effects on the performance of thrusters. Hence, facility effects of a large vacuum chambers are quite important to electric propulsion research. Cai *et al* recently investigated the facility effects of large vacuum chamber equipped with one-sided or two-sided cryopumps.[10,18,19] Some results related to these simulations are briefly listed as follows.

i). The background flow in large vacuum chambers such as LVTF is free molecular and quite complex. Figure 3 shows one DSMC simulation result of the average background flow number density and the average velocities along different stations of a long chamber.[10,18] There are one-sided vacuum pumps located on the right side of the chamber end, and the pump size is 40% of the chamber cross-section area. The pump sticking coefficient, $\alpha$, is set to 0.4 in the simulation. This figure indicates that the velocity and number density profiles in the large vacuum chamber are not constant and vary along different sections; especially at both chamber ends, there are large amounts of particles reflected back into the chamber center, either from chamber ends or vacuum pumps on the wall.

ii). The average background flow can be far from static.[10,18,19] The average background flow velocity can reach as high as 100 m/s for xenon and the background flow velocity distribution can not be considered to follow a Maxwellian distribution.[10,18,19]

ii). A full scale three-dimensional simulation of plasma plume flows inside a large vacuum chamber is quite expensive. By assuming a constant density distribution in a vacuum chamber equipped with one-sided or two-sided vacuum pumps, using the mass conservation law for the gas inside the vacuum chamber, the

following relation must hold:

$$\frac{d\rho}{dt} = \frac{d(\int \rho dv)}{Vdt} = \frac{1}{V}(\dot{m} - \frac{1}{4}\rho\alpha S_p\sqrt{\frac{8kT_w}{\pi m}}) \tag{22}$$

By using an initial boundary condition $\rho(t=0) = \rho_0$ and a steady state condition $d\rho(t\to\infty)/dt = 0$, the above equation yields one solution which consists of one unsteady term and one steady term:

$$\rho(t) = (\rho_0 - \sqrt{\frac{2\pi m}{kT_w}}\frac{\dot{m}}{\alpha S_p})\exp(-\frac{\alpha S_p}{V}\sqrt{\frac{kT_w}{2\pi m}}t) + \sqrt{\frac{2\pi m}{kT_w}}\frac{\dot{m}}{\alpha S_p} \tag{23}$$

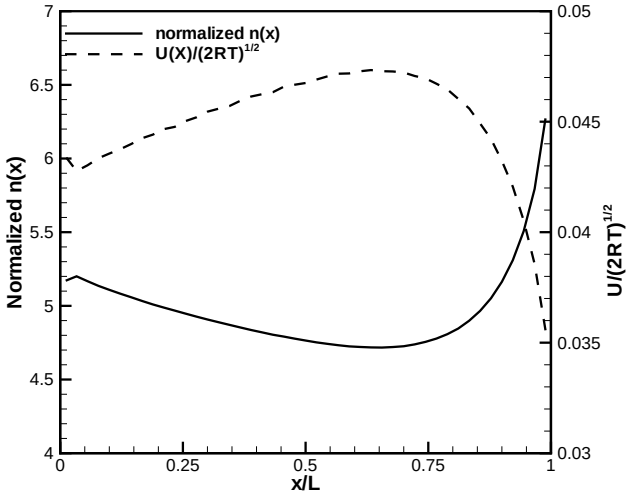


**Figure 3. 1D Number Density and Velocity Distribution along Chamber Axial Direction($S_p/S_c$=0.4, $\alpha$=0.4).**

It is evident from Equation 23 that if the pumps work efficiently, the decay of the unsteady term for density will result in a final flow state, however, Equation 23 also indicates that the unsteady term will take a finite time to decay significantly. For example, with the following LVTF parameters: $V$=280 $m^3$, $T_w$=300 K, $S_p$=7.26 $m^2$, and an assumption of $\alpha$=0.40, the decaying term is:

$$\rho_b(t) = C\exp(-0.57t) = C\exp(-t/1.75) \tag{24}$$

where $C$ is a constant.The significant term in this expression is the semi-decaying period $\tau_d$= 1.75 seconds. In experiments, usually the pumps operate for several hours, and steady background flows are well established. However, in particle simulations of the rarefied plasma plume flow field inside a vacuum chamber, usually the simulations develop as an unsteady process with a time step around $1\times10^{-7}$ second. This requires over 50 million time steps for three semi-decaying periods to reach a steady flow state. With a consideration that the discretization of a large chamber will require a large number of cells, a full three-dimensional simulation of the whole chamber flow is too expensive. In this study, the three-dimensional simulations are limited to a reduced scale of a cylindrical domain close to the thruster clusters. With this simplified approach to simulate the plume flow inside a vacuum chamber, the background flow must be properly estimated and included in the simulations.

iii). There are several key vacuum facilities effects that influence on the backpressure in a vacuum chamber, such as the vacuum pump sticking coefficient, $\alpha$, vacuum pump area, $S_p$, and chamber sidewall length, $L$.[10,18,19] Among these facility effects, the vacuum pump has the most important effects. For the experimental measurements in Ref.5, four two-sided cryogenic pumps in LVTF were operated. As pointed out by Biagioni[20], propellant frost will build up on cryopump surfaces and eventually will limit the pumping speed, hence, even though the nominal sticking coefficient for xenon-steel is high at 15 K, in real experimental operation, the sticking coefficient for pumps may be much lower. Hence, to accurately simulate a plume flow

in a vacuum chamber, whenever possible, parameters for the facility effects must be carefully decided with available experimental measurements data.

iv). The free molecular flow in LVTF, which is a large cylindrical chamber equipped with two-sided pumps, can be simplified and studied analytically.[10,18] The major principles for the analysis are based on the mass flow rates into the chamber from thrusters and that out of the chamber via cryopumps, flux relations along two directions and number density relations at various sections such as chamber ends and pumps. The major results of velocity distribution function, average velocity and average backpressure at the pre-pump region are:[10,18]

$$f(C) = \begin{cases} \frac{(2-s+\alpha s)n_{in}}{\alpha s(2-s)}\sqrt{\frac{m}{2\pi kT_w}}\exp(-\frac{m}{2kT_w}C^2), C>0 \\ \frac{(1-\alpha)\sqrt{T_w/T_p}n_{in}}{\alpha}\sqrt{\frac{m}{2\pi kT_p}}\exp(-\frac{m}{2kT_p}C^2) \\ +\frac{(1-s)(2-s-\alpha s)n_{in}}{\alpha s(2-s)}\sqrt{\frac{m}{2\pi kT_w}}\exp(-\frac{m}{2kT_w}C^2), C<0 \end{cases} \quad (25)$$

$$\frac{U}{\sqrt{2RT_w}} = \frac{\alpha s(2-s)}{\sqrt{\pi}(2-2s+\frac{1}{2}s^2+\frac{1}{2}\alpha s^2+(1-\frac{s}{2})(1-\alpha)s\sqrt{\frac{T_w}{T_p}})} \quad (26)$$

$$\frac{P_b S_c}{\dot{m}\sqrt{\gamma RT_w}} = \frac{1}{\alpha s(2-s)}\sqrt{\frac{\pi}{2\gamma}}(2-2s+\frac{1}{2}s^2+\frac{1}{2}\alpha s^2+(1-\alpha)s\sqrt{\frac{T_w}{T_p}}(1-\frac{s}{2})) \quad (27)$$

The sidewall length effect is important for long chambers,[10,18] and its influence can be considered by setting the temperature ratio to unity in the above relations. With this change, the formula for normalized pressure with $T_w/T_p$ =1 is:

$$\frac{P_b S_c}{\dot{m}\sqrt{\gamma RT_w}} = \sqrt{\frac{\pi}{2\gamma}}\frac{(2-2s+\frac{1}{2}s^2+\frac{1}{2}\alpha s^2+(1-\alpha)s(1-\frac{s}{2}))}{\alpha s(2-s)} \quad (28)$$

With known experimental measurement of backpressure and know pump size, the pump sticking coefficient, $\alpha$ can be decided with this equation.

With known facility parameters, a proper average background flow can be estimated. Experimental measurements[5] indicated there was a backpressure of $4.78 \times 10^{-4}$ Pa with four thrusters and four vacuum pumps ($s$=0.1460) in operation. With a mass flow rate of 0.833 mg/sec from each anode and 0.098 mg/sec from each cathode, the pump absorption coefficient computed from Equation 27 is 0.39, which is consistent with the conclusions obtained from analysis of other sets of experimental data[20,21] in LVTF. The mean background flow velocity computed with Equation 26 is about 6.0 m/sec with four thrusters and four pumps in operation.

With the above facility parameters, in the simulations in this study, a special of background flow is adopted. In the particle simulations, traditionally the most convenient treatment of background pressure is to adopt static background particles: inside each cell, there are a few particles with velocities sampled from a zero-centered Maxwellian velocity distribution function. These particles participate in collisions with normal particles and change the velocities of other particles, but their positions and velocities do not change. In this study, a similar background particle treatment is adopted with a few modifications. The number density calculated from Equations 27 is slightly less than the values obtained directly by $n = P_b/(kT_w)$, and their velocities are assigned from Equation 25, not a zero-centered Maxwellian distribution. There is a net average velocity towards the thrusters for the background particles. Because Equation 27 considers multiple factors from pumps such as the pump size and the sticking coefficient, thruster effects such as the mass flow rate, chamber effects such as the backpressure and properties of the propellant, it is reasonable to expect a more accurate result than the traditional treatment of background static particles.

## V. Simulations and Results

In this study, three DSMC-PIC particle simulations are performed to simulate plume flows from one, two and four BHT200 thrusters. Due to the setup symmetry, only one thruster is needed in the simulation and the results for cases with two and four thrusters in operation are obtained by symmetric reflections.

A specific PIC module is implemented in MONACO. Three unstructured meshes are generated with the software Hypermesh.[23] The very detailed geometries of the 7 mm conic protection cap and the small cathode

are included in the mesh. The cathode exit plane is an orifice with a diameter of $5.08 \times 10^{-4}$ m. The small size is a challenge for meshing and the circular cathode exit plane is simplified with six triangles by conserving the same exit area. Later simulation results indicate that the cathode has important effects on the flowfield, hence, the preservation of the cathode geometry is quite essential. All simulations use three static background particles per cell and all time steps are set to $2 \times 10^{-7}$ second.

Table 2 lists several details for these simulations. The finite element solver is called every 10 time steps for Equations 4, 8, 9 and takes a significant fraction of the simulation time. The simulations take 40,000 time steps to reach a steady stage and another 20,000 time steps for sampling. Several results are selected and discussed in groups as follows.

| Thrusters | Domain (cylinder) | Triangular cells | Tetrahedrons | Particles (million) | Time (Hours) | Machine |
|---|---|---|---|---|---|---|
| 1 | Full | 32,550 | 971,796 | $\tilde{9}.5$ | $\tilde{2}30$ | Parallel, 8 CPUs |
| 2 | 1/2 | 34,058 | 829,243 | $\tilde{8}.3$ | $\tilde{2}00$ | Parallel, 8 CPUs |
| 4 | 1/4 | 41,972 | 556,796 | $\tilde{5}.2$ | $\tilde{1}20$ | PC, 2.1GHz |

**Table 2. Simulation Details.**

## A. Comparison With Measurements

### *1. Electron Temperature*

Figure 4 shows contours of electron temperature with 4 thrusters in operation. With more thrusters in operation, the contours of electron temperature from single thrusters merge into one far downstream. Figures 5 and 6 show comparisons of electron temperature along several thruster centerlines and two cluster centerlines. It is significant to mention that the Boltzmann relation assumes a constant electron temperature and cannot predict any variation. The detailed fluid electron model yields a non-constant electron temperature field which is more physically reasonable. The circles represent experimental measurements along the centerline of a thruster acceleration channel with one thruster in operation. The solid line represents the corresponding simulation result with one thruster in operation. The comparison indicates that the numerical simulation results are close to the experimental measurement data. It is also evident that with several thrusters in operation, the centerline electron temperature is slightly different in the near field and has a large difference in the far field. With more thrusters in operation, cluster centerline values and thruster centerline values merge at a short distance from the thrusters, correspondingly. The closer to the thruster exit, the higher the electron temperature, and the simulation results predict that the electron temperature from different plumes merge at station X=0.08 m. The experimental data was obtained with a triple Langmuir probe. This is one of the most important results in this study because these results clearly indicate the superiority of the detailed electron model over the Boltzmann relation, and it clearly displays the clustering effects as well.

### *2. Plasma Potential*

Figure 7 shows contours of plasma potential in the plane y=0 with 4 thrusters in operation. In the near field, the plumes are well separated while at a short distance from the thruster exit plane they merge into one plume. Compared with the electron temperature results, the plasma potential merges at a further downstream station, X=0.15 m.

Figures 8, 9 and 10 present comparisons of plasma potential along different centerlines and at the station x=0.05 m. The experimental data in these three pictures were obtained with two thrusters in operation. Figure 10 shows that the plasma potentials along different centerlines converge into one universal distribution at about X=0.15 m, which indicates that the four or two plume flows merge into one. These two figures also indicate that the numerical simulation predicts lower potential peak values than the experimental measurements at specific locations. However, they predict a matching distribution along the centerline passing through the middle point of two thrusters, and the general shape of the computed potential profile at X=0.05 m fits the experimental measurement as well.

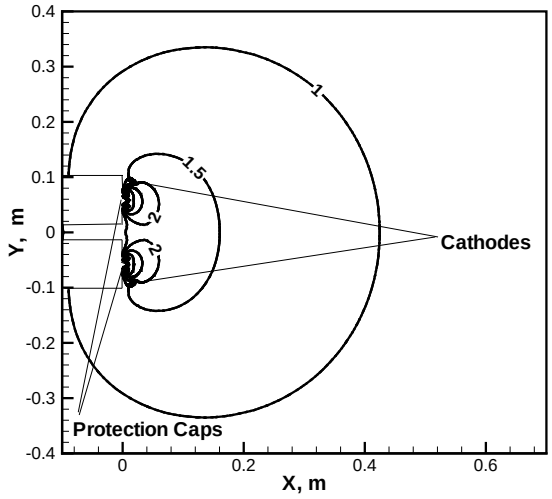


**Figure 4. Contours of Electron Temperature (eV) in the Plane Through Thrusters 3 and 4 (increment=0.5 eV, 4 Thrusters in Operation).**

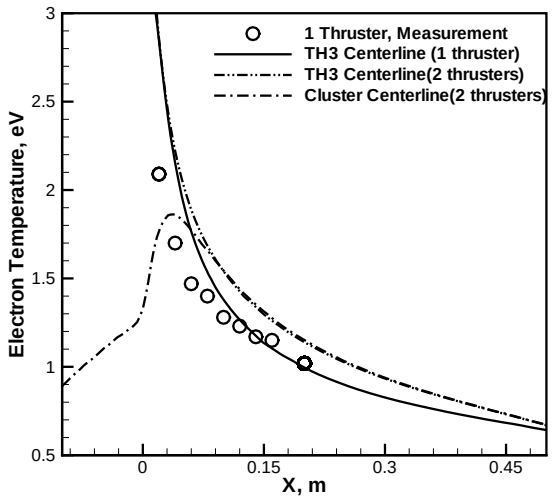


**Figure 5. Profiles of Electron Temperatures (eV) along Different Centerlines(I).**

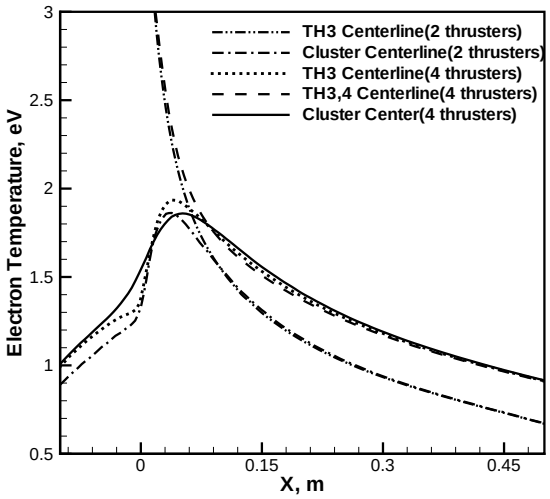


**Figure 6. Profiles of Electron Temperatures (eV) along Different Centerlines(II).**

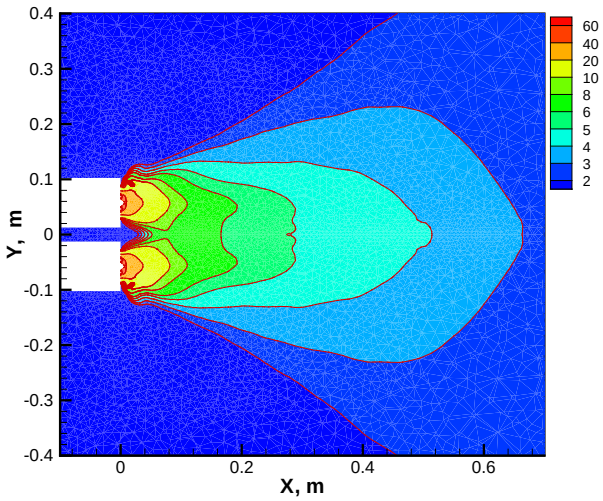


**Figure 7. Contours of Plasma Potential(V) in a Plane Through Thrusters 3 and 4 (4 Thrusters in Operation).**

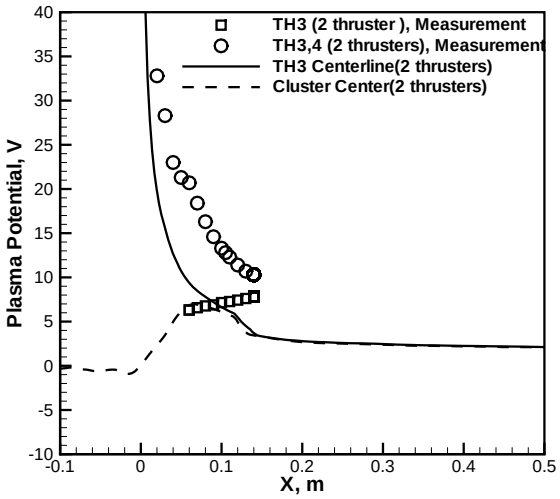


**Figure 8. Profiles of Plasma Potential (V) along Centerlines(I).**

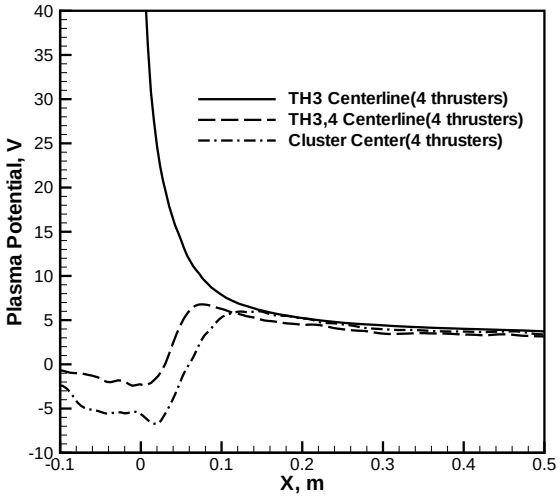


**Figure 9. Profiles of Plasma Potential (V) along Centerlines(II).**

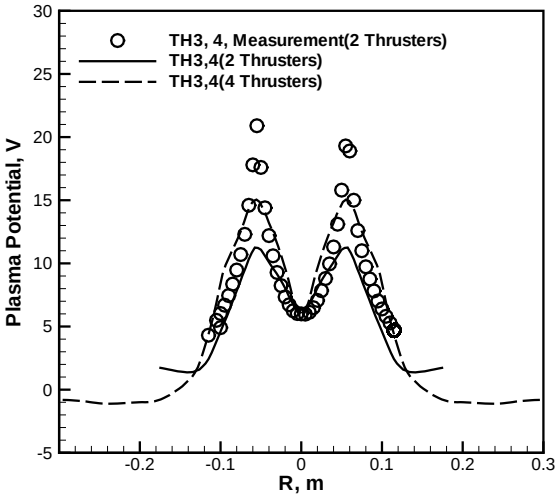


**Figure 10. Plasma Potential(V) at Station X=5 cm and through the Horizontal line.**

*3. Electron Density*

Figures 11 and 12 show electron number densities along different centerlines and at station X=0.20 m, respectively. Figure 11 indicates that the number densities from all four plumes merge into one at the station around X=0.20 m while two plumes merge into one at the station around X=0.50 m. Electron number density obtained from a Langmuir probe always contains the greatest experimental uncertainty.[3] Three different profiles of measured data are shown representing two different corrections to the raw data.[3] The profile labeled "sheath" assumes that the probe collection radius is increased by a sheath of five Debye lengths, thus leading to a reduction in plasma density. The profile labeled "Laframboise" incorporates corrections due to the slightly different voltages applied to each of the three probes in the instrument. The correction is sensitive to the ratio of electron to ion temperature, and a ratio of one is assumed in the corrected data shown here. Comparisons indicate that in general the numerical results predict significantly lower values than the experiments. However, the sheath and Laframboise corrected data yield better agreement with the simulation data.

## B. Clustering Effects

Clustering effects are illustrated by the near field ion number density. Figure 13 shows the ion number density at station x=2 cm with 4 thrusters in operation. Note that the contour increments are not uniform in this result. This figure indicates that with a cluster of four thrusters in operation, a special three-dimensional structure results in the ion number densities. With two thrusters in operation, the middle point between the two thrusters is a saddle point which has a lower potential than the plume core, but a higher potential value than the far field. Hence, slow ions diffuse along all directions, there exists two spots close to the cathodes with relatively high density of slow ions due to the CEX effects. With four thrusters in operation, the topographic pattern of ion density in the near field is quite different. The four thruster centers represent high potential values because of large amount of ions in the plume cores. When CEX happens, particles may freely diffuse away along the electric field direction opposite to the cluster center, hence low ion densities exist along four major diffusion directions of 45 degree, 135 degree, 225 degree and 315 degree, as indicated by Figure 13. A fraction of slow ions may travel along the electric field direction to the cluster center, which has a relatively lower potential value than the plume core and a zero value of electric field. These four plume beams result in a cusp shape of low potential field in the middle that traps a large amount of slow CEX ions. There are slow ions coming from the four thruster plume beams into the center region, and at the same time, there are slow ions escaping from the center via two paths. The first path is shown in Figure 13 via the four low potential gaps between the thrusters, i.e. 0 degree, 90 degree, 180 degree and

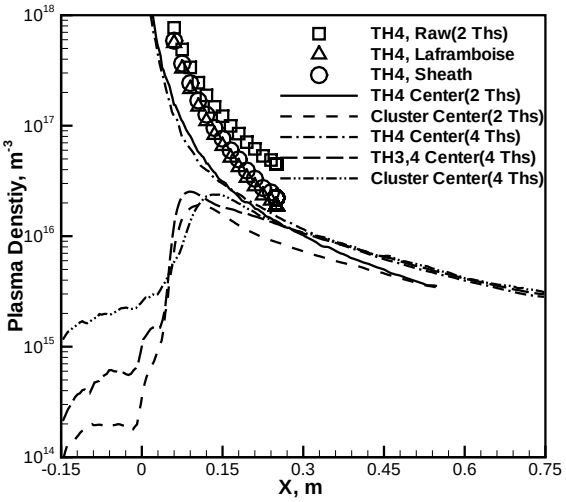


**Figure 11. Profiles of Electron Density ($m^{-3}$) along Different Centerlines.**

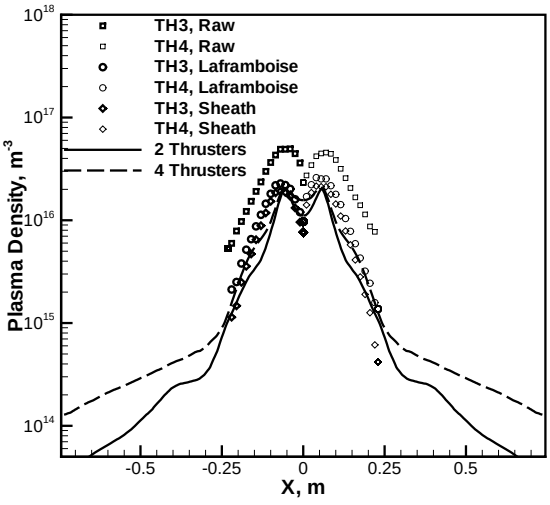


**Figure 12. Profiles of Electron Density ($m^{-3}$) at Station X=20 cm and Two Thruster Centerlines.**

270 degree. At this station, these escaping slow ions form a special pattern of a four-leaved clover. There are four small secondary leaves in the contours as well, which are generated by the cathode. A relatively large amount of slow ions are created around the cathodes, without electric field effect, they should diffuse upwards or downwards. However, with the effects of the electric field, these slow ions diffuse along the four directions with the strongest electric field strength: 45 degree, 135 degree, 225 degree and 315 degree. In the near field, a special topography is formed: four strong plume cores plus a secondary high potential at the cluster center, 4 major leaves and 4 secondary leaves represent diffusion directions for the slow ions. Further downstream, the strengths of the ion beams decrease rapidly and eventually merge into one plume. Figure 13 illustrates the CEX effects, clustering effects and cathode effects. In the corresponding neutral number density contours, no special patterns are observed. The second path that the slow ions can escape

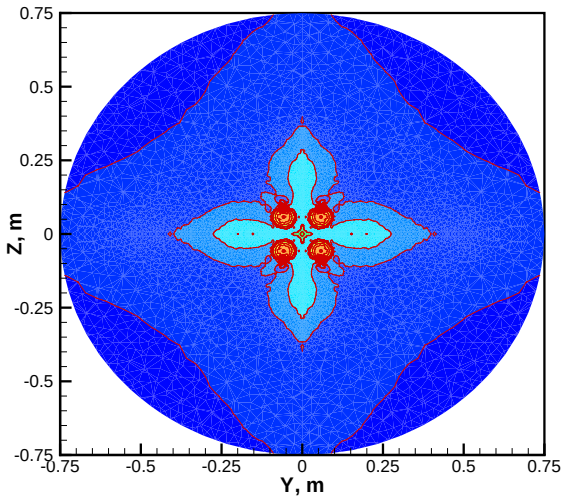


**Figure 13. Contours of Ion Number Density ($m^{-3}$) at Station X=2 cm (4 Thrusters in Operation).**

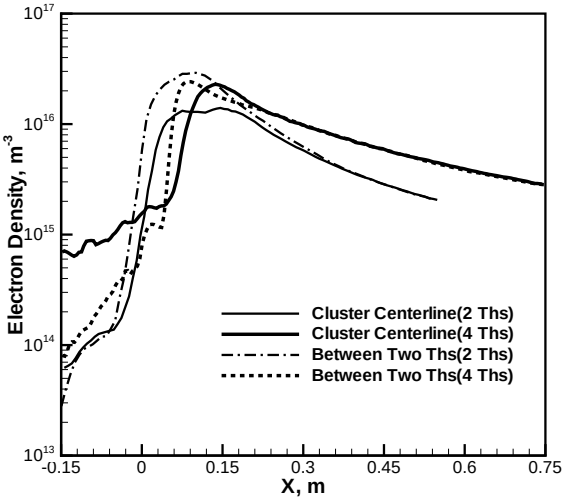


**Figure 14. Distribution of Electron Number Density ($m^{-3}$) along Lines Passing through the Cluster Center and Midpoint of Two Thrusters(Two or Four Thrusters in operation) .**

along from the cluster center is backwards to the back of the thruster. Figure 14 shows the comparison of ion

number density along two horizontal lines passing through the cluster center and the middle of two thrusters with two and four thrusters in operation. It is evident that with four thrusters in operation there is a higher number density of slow ions behind the thrusters. A fraction of slow ions originally diffusing radically are trapped in the middle of the four plume beams, as a result of the electric field, a fraction of these trapped slow ions diffuse through the gaps between the plumes, forming the clover shape, while another fraction of slow ions diffuses horizontally. Hence a high level of ion impingement is expected at the back of the thrusters when four thrusters are in operation.

### C. Cathode Effects

Cathode effects can be illustrated by velocity and number density contours. Figures 15- 16 show several contours of ion and atom velocity in a vertical plane that includes the cathode for one and two thrusters in operation. These figures illustrate that the cathode has several effects on the ion and atom velocity distributions. The existence of a cathode in all of these plots result in "erosion" areas around the cathodes. In the near field close to the thruster exit, the ion velocity is accelerated by the strong electric field, while further down stream, the ion velocity changes slowly because of CEX effects. The neutral density around the thruster is high, but quickly decreases in all directions. With a decreasing percentage of slow neutrals, the percentage of fast neutrals, as a result of CEX effects, increases at the same time. As a net effect, the neutral velocity is accelerated downstream.

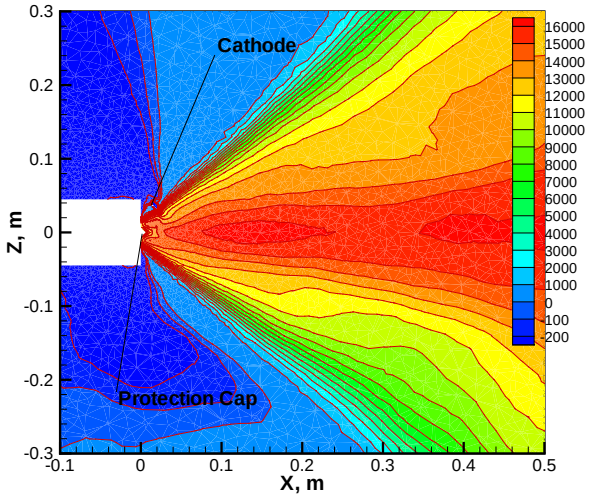


**Figure 15. Contours of Ion Velocity($m/s$) along X Direction Passing Through Thruster 1 (1 Thrusters in Operation).**

Figure 17 shows the ion number density contours in the plane y=0 with one thruster in operation. This plane intersects the 7 mm conic protection cap and the cathode. This figure indicates that there is a high ion number density accumulated next to the protection cap. The bulges in the outer region of the contours close to the thrusters result from the CEX effects and a large density of slow ions exists in these regions. This figure evidently indicates the cathode effects because of the asymmetry in the bulges. Another observation is that the value of ion number density around the cathode is much higher than the value from the anode. Though these simulations include the ion flux from the cathodes, the flux amount is quite small. The physical explanation for this phenomenon is that neutrals emitted by the cathode collide with the plume beam, with the CEX effects, and one fraction of the slow ions reflects upward and forward. Figure 18 clearly shows the cathode effects in the neutral number density as well.

### D. Analysis of Neutral Flow

The neutral number density can be predicted with a simple free molecular flow model. Because the neutral flow is highly rarefied, the Knudsen number for neutrals is about 55 for a channel height of 7.5 mm. Hence

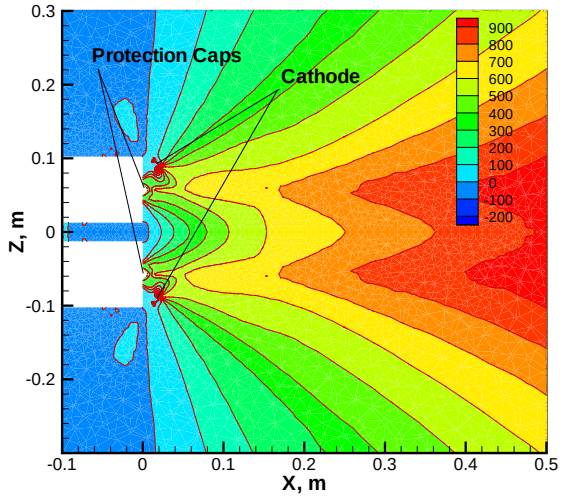


**Figure 16. Contours of Neutral Velocity($m/s$) along X Direction Passing Thrusters 3 and 4 (2 Thrusters in Operation).**

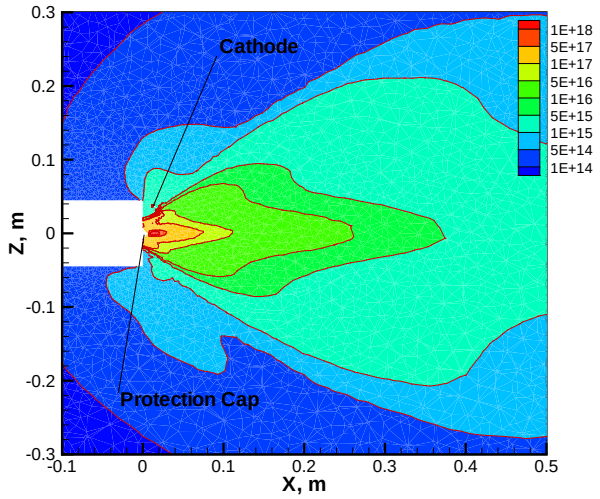


**Figure 17. Contours of Ion Number Density ($m^{-3}$) in the Plane through Thruster 1 (1 Thruster in Operation).**

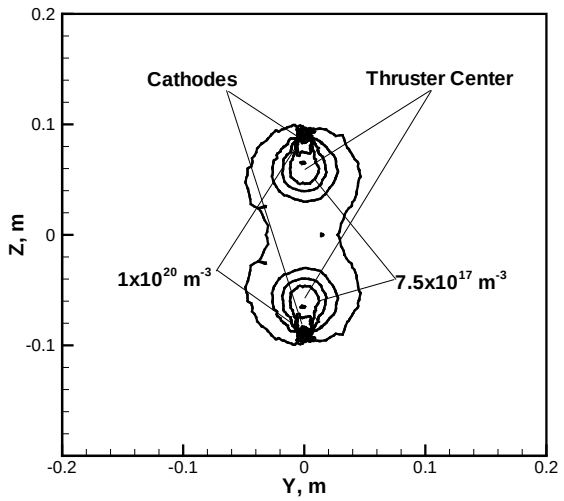


**Figure 18. Contours of Neutral Number Density ($m^{-3}$) at Station X=2 cm (2 Thrusters in Operation).**

the neutral number density distribution, with four thrusters in operation, can be approximated by a free molecule flow model with zero mean velocity from four small annular sources for the thrusters and four small orifices for the cathodes. At any specific point with coordinates $(x, y, z)$ in front of the thrusters, the velocity phase at that point can only have non zero values within specific solid angles from the four ring sources of thrusters and four small orifices for the cathodes. The number density distribution at that point can be estimated by the solid angles at that point subtended by these four ring sources and four cathodes. The derivation process is straightforward but tedious and the final expression for the solid angle is listed in the Appendix. With the same principle, recently Cai studied several problems of free molecular flow out of exits with different shapes.[10]

With four thrusters in operation, the final expression for the number density at any point in front of the thruster cluster is:

$$\begin{aligned} n(x,y,z) = \quad & n_{back} + \tfrac{x(R^2-r^2)n_a}{4\pi}(F(A_1,A_2)+F(A_3,A_4)+F(A_5,A_6)+F(A_7,A_8)) \\ & +\tfrac{n_c}{4\pi}(H(n_{x1},n_{y1},n_{z1},b,a,d)+H(n_{x2},n_{y2},n_{z2},b,-a,d) \\ & +H(n_{x3},n_{y3},n_{z3},b,-a,-d)+H(n_{x4},n_{y4},n_{z4},b,a,-d) \end{aligned} \tag{29}$$

With two thrusters or one thruster in operation, the corresponding results are a fraction of Equation 29.

Figure 19 presents the comparison between the simulation results and the analytical results along different centerlines with 4 thrusters in operation. Both the simulation results and the analytical results present the same trends: The neutral number density along the cluster centerline and the centerline of vertical/horizontal planes first increases quickly then decreases slowly with a maximum value at a specific distance from the thruster; the maximum value along the cluster centerline is further downstream from the thruster face and is smaller than the value on the centerline between two thrusters. The difference between simulation and analytical results can be explained by the following factors omitted in this crude analytical model: wall effects, the MEX and the CEX effects and the non-zero mean velocity at the exit planes of anodes and cathodes. Especially, the wall effect is significant in the very near field because the thruster wall area is large, and the non-zero average speed may have significant effects as well. Despite these factors, the comparison still yields a certain agreement.

### E. General Comments

The first comment is about the drawbacks of axi-symmetric simulations. Firstly, with more than one thruster in operation, axi-symmetric simulation is completely not applicable. Secondly, in simulation of a single thruster, the three-dimensional cathode is usually either completely omitted or simplified as an annular

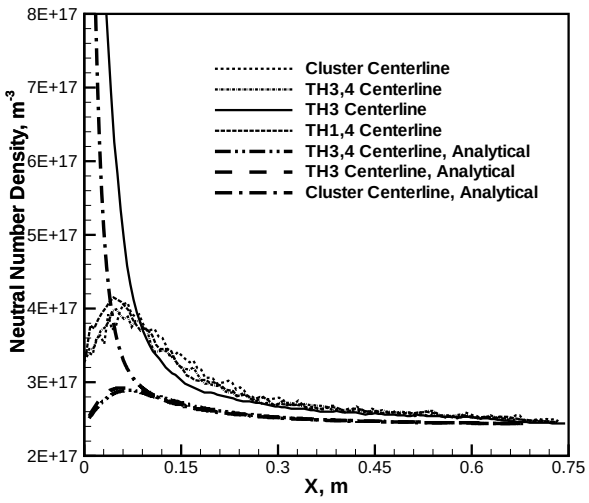


**Figure 19. Distribution of Neutral Number Density ($m^{-3}$) along Different Centerlines(4 Thrusters).**

source in axi-symmetric simulations. However, from this study, it is evident that the cathode position, angle, and amount of flux have significant effects on the flowfield of neutrals. Hence, though much expensive and complex, these three-dimensional simulations are superior over axi-symmetric simulations.

The second comment is about future work. One defect for these three-dimensional simulations which should be addressed is the adoption of linear finite element in the present study. For the right hand side terms in Equations 4, 8 and 9, several second order derivatives are involved, but the finite element adopted in this study employs a linear element. Equation 8 is mostly affected by this problem. For three-dimensional simulations, the average mesh density is much sparser than the mesh in the axi-symmetric simulations, hence, this problem is much important. Due to the mesh density, the simulation of four thrusters is the most successful because of a relatively high density of cells. This problem is ameliorated because the derivative calculation scheme in this study permits a degree of resolution for these second derivatives, and the source term is weak. The second future work is an addition of magnetic field effects into the simulation package.

## VI. Conclusions

In this study, a comprehensive three-dimensional DSMC-PIC package with a general purpose finite element solver and a detailed electron fluid model was developed and applied to simulate the plasma plumes from a cluster of four Hall thrusters with different numbers of thrusters in operation. Several major implementation issues were reviewed and the backpressure was modeled with full considerations of facility effects of large vacuum chambers.

Generally, the simulation results successfully yield some detailed three-dimensional flow patterns, and most results matched the available experimental measurements or analytical results. Different plume flow properties merge at different downstream locations. The cluster effects are evidently captured. The simulation also showed that the cathodes have significant effects on the near field properties. The CEX effect is clearly illustrated in the simulation results as well.

## Appendix

$$
\begin{aligned}
\Omega = & \sum_0^4 \int \frac{x}{R_i^3} ds_i + \sum_0^4 \int \frac{(x-b)n_{xj}+(y-a_i)n_{xj}+(z-d_j)n_{xj}}{R_j^3} ds_j \\
= & \sum_{i=0}^4 \int_0^{2\pi} \frac{x}{R_i^3} d\theta + \sum_0^4 \int \frac{(x-b)n_{xj}+(y-a_i)n_{xj}+(z-d_j)n_{xj}}{R_j^3} ds_j \\
= & \frac{x(R^2-r^2)}{2} \int_0^{2\pi} \frac{d\theta}{(x^2+(y-(a+\frac{R+r}{2}\cos\theta)^2+(z-(a+\frac{R+r}{2}\sin\theta)^{3/2}} \\
& + \frac{x(R^2-r^2)}{2} \int_0^{2\pi} \frac{d\theta}{(x^2+(y-(-a+\frac{R+r}{2}\cos\theta)^2+(z-(a+\frac{R+r}{2}\sin\theta)^{3/2}} \\
& + \frac{x(R^2-r^2)}{2} \int_0^{2\pi} \frac{d\theta}{(x^2+(y-(a+\frac{R+r}{2}\cos\theta)^2+(z-(-a+\frac{R+r}{2}\sin\theta)^{3/2}} \\
& + \frac{x(R^2-r^2)}{2} \int_0^{2\pi} \frac{d\theta}{(x^2+(y-(-a+\frac{R+r}{2}\cos\theta)^2+(z-(-a+\frac{R+r}{2}\sin\theta)^{3/2}} \\
& + H(n_{x1}, n_{y1}, n_{z1}, b, a, d) + H(n_{x2}, n_{y2}, n_{z2}, b, -a, d) \\
& + H(n_{x3}, n_{y3}, n_{z3}, b, -a, -d) + H(n_{x4}, n_{y4}, n_{z4}, b, a, -d) \\
= & x(R^2-r^2)(F(A_1, A_2) + F(A_3, A_4) + F(A_5, A_6) + F(A_7, A_8)) \\
& + H(n_{x1}, n_{y1}, n_{z1}, b, a, d) + H(n_{x2}, n_{y2}, n_{z2}, b, -a, d) \\
& + H(n_{x3}, n_{y3}, n_{z3}, b, -a, -d) + H(n_{x4}, n_{y4}, n_{z4}, b, a, -d)
\end{aligned}
$$

where

$$
H(n_x, n_y, n_z, b, a, d) = \begin{cases} \frac{\pi R_c^2((x-b)n_x+(y-a)n_y+(z+b)n_z)}{((x-b)^2+(y-a)^2+(z+d)^2)^{3/2}}, (x-b)n_x+(y-a)n_y+(z-d)n_z > 0 \\ 0, (x-b)n_x+(y-a)n_y+(z-d)n_z < 0 \end{cases}
$$

$$
F(A_i, A_j) = E(\sqrt{\frac{2A_j}{A_i+A_j}})/(A_i+A_j)^{3/2}
$$

$E(x)$ is the complete elliptical integrals, and

$$
\begin{aligned}
A_1 &= (y-a)^2 + (\tfrac{R+r}{2})^2 + x^2 + (z-a)^2, A_2 = (R+r)\sqrt{(y-a)^2+(z-a)^2} \\
A_3 &= (y+a)^2 + (\tfrac{R+r}{2})^2 + x^2 + (z-a)^2, A_4 = (R+r)\sqrt{(y+a)^2+(z-a)^2} \\
A_5 &= (y-a)^2 + (\tfrac{R+r}{2})^2 + x^2 + (z+a)^2, A_6 = (R+r)\sqrt{(y-a)^2+(z+a)^2} \\
A_7 &= (y+a)^2 + (\tfrac{R+r}{2})^2 + x^2 + (z-a)^2, A_8 = (R+r)\sqrt{(y+a)^2+(z+a)^2}
\end{aligned}
$$

The above derivation process uses the elliptical calculus formula[24]:

$$
\int_{-\pi/2}^{\pi/2} \frac{d\theta}{(a+b\sin\theta)^{3/2}} = \frac{2}{(a+b)^{3/2}} E(\sqrt{\frac{2b}{a+b}})
$$

## Acknowledgments

This work is supported by the Air Force Office of Scientific Research through Grants F49620-03-1-0123 and FA9550-05-1-0042. The authors gratefully acknowledge the contributions to this work by Dr. Brian Beal and Dr. Mitchell Walker for sharing their experimental data.

## References

[1]Bird, G.A., *Molecular Gas Dynamics and the Direct Simulation of Gas Flows*, Clarendon Press, New York, 1991.

[2]Birdsall, C.K., and Langdon, A.B., *Plasma Physics Via Computer Simulation*, Adam Hilger, New York, June 1991.

[3]Boyd, I. D. and Yim, J.T., "Modelling of the Near Field Plume of a Hall Thruster," *Journal of Applied Physics*, Vol. 95,2004, pp.4575-4584.

[4]Hargus, W.A. and Reed, G., "The Air Force Clustered Hall Thruster Program," AIAA Paper 2002-3678, July 2002, Indianapolis, IN.

[5]Beal, B.E., "Clustering of Hall Effect Thrusters for High-Power Electric Propulsion," Ph.D. Dissertation, Aerospace Engineering Dept., the Univ. of Michigan, Ann Arbor, MI, 2004.

[6]Ahedo, E., Martinez-Cerezo, P., and Martinez-Sanchez, M., "One-dimensional Model of the Plasma Flow in a Hall Thruster," *Physics of Plasma*, Vol. 8, 2001, pp.3058-3068.

[7]Mitcher, M., and Kruger, C.H., *Partially Ionized Gases*, Wiley, 1973.

[8]Vichnevetsky, R., *Computer Methods for Partial Differential Equations*, Prentice-Hall, New Jersey 1981.

[9]Press, W.H., Teukolsky, S.A., Vetterling, W.T. and Flannery, B.P., *Numerical Recipes in C*, 2nd edition, Cambridge University Press, Cambridge, UK, 1999.

[10]Cai, C., "Theoretical and Numerical Studies of Plume Flows in Vacuum Chambers," Ph.D. thesis, Department of Aerospace Engineering, University of Michigan, October 2005.

[11]Ruyten, W.M., "Density-conserving shape factors for particle simulations in cylindrical and spherical coordinates," *Journal of Computational Physics*, Vol. 105, 1993, pp.224-232.

[12]Hammel, J.R., "Development of An Unstructured 3-D Direct Simulation Monte Carlo/Particle-In-Cell code and the Simulation of Microthruster Flows," M.S. Dissertation, Mechanical Engineering Dept., Worcester Polytechnic Institute, Worcester, MA, 2002.

[13]Dalgarno, A., McDowell, M.R.C, and Williams, A., "The Mobilities of Ions in Unlike Gases," Proceedings of the Royal Society, Vol. 250, 1958, pp411-425.

[14]Pullins, S.H., Chiu, Y., Levandier, D.J. and Dresseler, R.A., "Ion Dynamics in Hall Effect and Ion Thruster -Xenon Symmetric Charge Transfer," AIAA Paper 2000-0636, Jan. 2000, Reno, NV.

[15]Miller, S., Levandier, D.J., Chiu, Y., and Dressler, R.A., "Xenon Charge Exchange Cross Sections for Electrostatic Thruster Models," *Journal of Applied Physics*, Vol. 19, 2002, pp.984-991.

[16]Boyd, I.D., "Conservative Species Weighting Scheme for the Direct Simulation Monte Carlo Method." *Journal of Thermophysics and Heat Transfer*, Vol.10, No.4, pp579-585, 1996.

[17]Dietrich, S. and Boyd, I. D., "Scalar and Parallel Optimized Implementation of the Direct Simulation Monte Carlo Method," *Journal of Computational Physics*, Vol. 126, p. 328, 1996

[18]Cai, C., Boyd, I.D. and Sun, Q., "Free Molecular Background Flow in a Vacuum Chamber Equipped with Two-Sided Pumps," *Journal of Vacuum and Technology (A)*, Jan-Feb, 2006.

[19]Cai, C., Boyd, I.D. and Sun, Q., "Rarefied Background Flow in a Vacuum Chamber Equipped with one-Sided Pumps," *Journal of Thermophysics and Heat Transfer*, to be published.

[20]Biagioni,L., Boccaletto,L., Marcuccio,L., Nicolini,S., Servi, D. and Andrenucci, M., "A Large Space Simulator for Electric Propulsion Testing: Design Requirements and Engineering Analysis," AIAA Paper 2000-3750, July 2000.

[21]Walker, M.W., Gallimore,A.D., Boyd I.D. and Cai C., "Vacuum Chamber Pressure Maps of a Hall Thruster Cold-Flow Expansion," *Journal of Propulsion and Power*, Vol.20, No.6, pp1127–1131, 2004.

[22]Walker, M.W., "Effects of Facility Backpressure on the Performance and Plume of a Hall Thruster," Ph.D. thesis, Department of Aerospace Engineering, University of Michigan 2004.

[23]HyperMesh, Ver.6.0, Altair Engineering Inc., Troy, MI, 2003.

[24]Byrd, P. and Friedman, M., *Handbook of Elliptic Integrals For Engineers and Physicists*, Springer-Verlag, 1954, pp173.